ADVANCED ENGINEERING MATERIALS
www.aem-journal.com

Fabrication of High Aspect-Ratio Surface Micro Patterns on Stainless Steel using High-Speed Direct Laser Interference Patterning

Valentin Lang, Bogdan Voisiat, Tim Kunze, and Andrés Fabián Lasagni*

This work addresses the fabrication of periodic micro patterns on stainless steel by means of Direct Laser Interference Patterning. A modular optics assembly is introduced which produces two-beam interference patterns within a 5 × 100 μm rectangular shaped laser spot. The optical assembly considers optimal utilization of the available laser power in order to enable high processing rates. Using different optical elements, the spatial period of the periodic structures was set to 8 μm and 19 μm. The effect of the processing parameters on the morphology of the produced patterns is investigated by means of confocal microscopy, scanning electron microscopy, and energy-dispersive X-ray spectroscopy. It is found that the pulse repetition rate shows a strong influence on the structure height accompanied by considerable heat accumulation effects, which is reported for the first time for this method. In addition, aspect ratios slightly higher than one could be realized, which is also reported for the first time when using Direct Laser Interference Patterning with ns-pulsed lasers. Particularly for the smaller periods, the melt flow impairs pattern formation due to the overmelting of the material (humping). Moreover, variations of the surface chemistry are observed, especially for higher accumulated laser fluences.

1. Introduction

It is well known that periodic micro-patterns on surfaces can influence and improve different properties. A prominent example is the shark skin, which has shown that repetitive surface patterns with feature sizes on the micrometer scale can significantly reduce drag (friction between the fluid and the surface).[1–3] These surface features have been successfully reproduced in different materials, including steels,[4,5] polymer,[6] acrylic,[7] and textiles.[8] Other bio-inspired examples are self-cleaning surfaces such as the lotus leaf, where tailored topographies with micro- and nano-features lead to super-hydrophobic properties.[9–11] In medical technology, the biocompatibility of implants in the human body has been improved by well-defined surface textures with surface roughness's from some tens of nanometers[12–14] up to several micrometers.[15,16] In addition, microstructures are known to reduce the bacterial adhesion,[17] which permits prevention of serious infections (for example with Staphylococcus,[18–20] *Escherichia coli*,[19,20] *Pseudomonas aeruginosa*,[19] *Pseudomonas fluorescens*,[21] and diatom attachment[22]). In the field of large-area optical applications, such as organic light emitting diodes (OLED)[23–25] or photovoltaic devices,[26–28] well-controlled diffraction effects introduced by micro-gratings are used to improve their efficiencies. The height of the periodic topography features (respectively the aspect ratio) is often of key importance for the surface function.[29–31]

Nowadays, various methods are available for the fabrication of high-resolution micro-patterns down to the nanometer scale such as lithography or electron beam technologies. They typically require high invest and operation costs accompanied by restrictions on component dimensions and geometry as well as low processing speeds. Consequently, there is a lack on industrially-relevant one-step methods permitting high processing speeds.

Direct Laser Interference Patterning (DLIP) technology has turned out as a cost-efficient tool for the mass production of surface structures in the micrometer and submicrometer range.[32] The DLIP technology takes advantage of a periodic intensity distribution, obtained from two or more superimposed coherent beams. In the case of two-beam interference, a line-like intensity pattern is obtained where the spatial period Λ is typically defined by the used laser wavelength λ and angle of incidence α between impinging laser beams, as shown in Equation (1).

$$\Lambda = \frac{\lambda}{2 \cdot \sin^{\alpha}/_{2}}. \quad (1)$$

This allows resolutions below those of conventional methods such as micro milling[33,34] or direct laser writing.[35]

V. Lang, Dr. B. Voisiat, Prof. A.F. Lasagni
Technische Universität Dresden
George-Bähr-Strasse 3c
01069 Dresden, Germany
E-mail: valentin.lang@tu-dresden.de

V. Lang, Dr. T. Kunze, Prof. A.F. Lasagni
Fraunhofer-Institut für Werkstoff- und Strahltechnik (IWS)
Winterbergstraße 28, 01277 Dresden, Germany

The ORCID identification number(s) for the author(s) of this article can be found under https://doi.org/10.1002/adem.201900151.

DOI: 10.1002/adem.201900151

The use of short pulse lasers (pulse duration >1 ns) results in a considerable amount of melting of the substrate material due to heat diffusion. As a result, the topographies achievable with DLIP using ns-pulsed lasers are generally limited in their aspect ratios (ratio between structure depth and spatial period) to up to 0.5.[36] While high-aspect-ratio structures are already possible using ps pulsed lasers in combination with the DLIP technology,[37] ns laser sources are still very interesting for industrial high-speed structuring applications due to the lower invest costs and higher available laser powers. Thus, there is a demand for structuring solutions to structure metals with higher aspect ratios using DLIP with ns-pulsed lasers.

This work focuses on the high-speed structuring of stainless steel employing ns-pulsed laser radiation using DLIP. In addition, for the first time, heat accumulation during the DLIP process is investigated when utilizing ns laser pulses. Rectangular shaped laser spots permit high surface processing rates by enabling the treatment of larger surface areas per laser pulse.[38,39] Therefore, an optical DLIP setup is designed, permitting to form the interfering laser beams into a rectangular shape containing a well-defined interference pattern. A similar approach has been already successfully applied to achieve exceptionally high structuring speeds close to $1\,m^2\,min^{-1}$.[40] By using different optical elements, the spatial period of the micro-structures was set to 8 and 19 µm. The influence of the processing parameters (laser fluence, repetition rate, feed speed) on the morphology of the produced patterns is investigated. Additionally, the melt flow characteristics as a result of heat accumulation as well as the amount of molten material are taken in account. The obtained surfaces are examined by Confocal Microscopy (CFM) and Scanning Electron Microscopy (SEM). Moreover, energy dispersive X-ray spectroscopy (EDX) measurements are also performed in order to determine possible changes in the chemistry of the treated surface.

2. Experimental Section

2.1. Materials

Stainless steel substrates (1.4031, X5CrNi18-10) with a thickness of 0.9 mm were electro-polished obtaining a surface roughness (Sa) of 53 nm. Before the laser experiments, the metallic substrates were cleaned using a lint-free cellulose paper with isopropyl alcohol.

2.2. Direct Laser Interference Patterning

The laser experiments were carried out using a nanosecond pulsed slab-shaped solid-state laser (Edgewave IS400) operating at its fundamental wavelength λ of 1064 nm. This system permits to change the repetition rate from single pulse to 10 kHz, with a maximum average power of 150 W (@ 10 kHz repetition rate). The pulse duration τ was 10 ns. In the performed experiments, the laser fluence was kept constant at $3.2\,J\,cm^{-2}$. This can be done by setting the pulse energy to 16 mJ (at the materials' surface) considering that the area which is irradiated by each laser pulse is $0.1 \times 5\,mm^2$. In consequence, depending on the used repetition rate, the laser power level was adjusted in order to keep this value constant, considering optical losses in the beam path of ≈33% (0.1 kHz: 2.4 W, 1 kHz: 24.2 W, 2 kHz: 48.4 W, 5 kHz: 121 W).

The interference patterns were generated using an optical assembly developed by Fraunhofer IWS (see **Figure 1**). By using two bi-prisms, the laser beam is split into two sub-beams which are overlapped on the sample surface. Additionally, the laser beams are formed into a rectangular shape of 5 mm x 100 µm on the sample surface by first expanding the laser beam in one spatial direction with a cylindrical telescope, and secondly focusing the sub-beams one-dimensionally with an additional cylindrical lens (see Figure 1). The intersection angle between

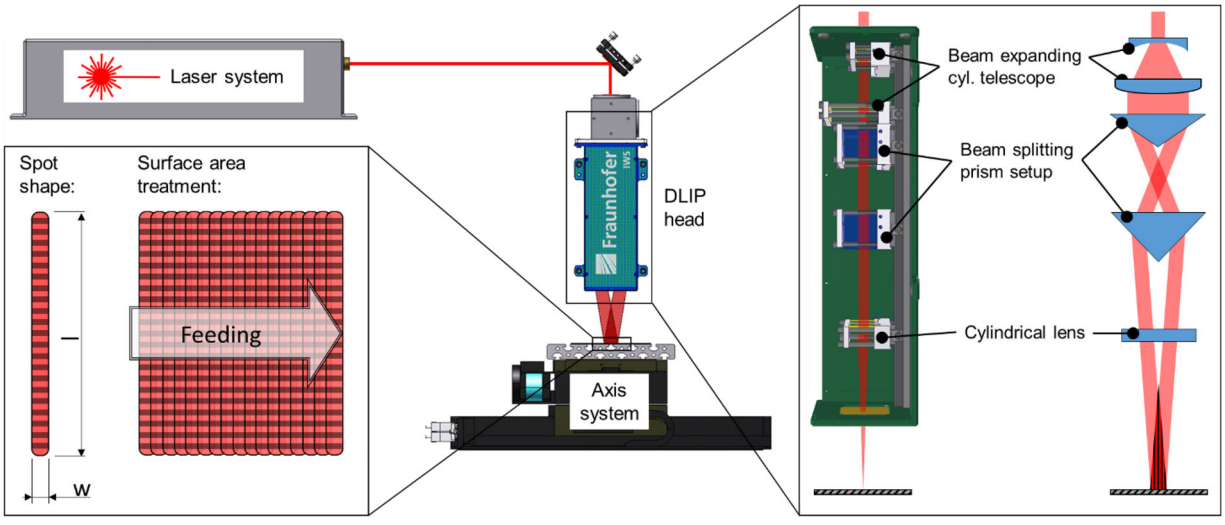

Figure 1. Experimental setup (center) illustrating the optical assembly (right side) that forms the line-like shaped irradiation area containing a two beam interference pattern and the areal scanning strategy (left side).

the overlapping sub-beams is defined by the wedge angles of the bi-prisms. In this work, the spatial periods Λ of 8 µm and 19 µm were used, which corresponds to intersection angles α of 7.6 and 3.1, respectively.

In order to structure larger areas, the relative movement between the laser irradiated area (which contains the interference pattern) and the sample surface was performed using a linear stage. The surface processing rate A' is determined by the length l of the laser irradiated area per pulse and the feed rate v, as shown in Equation (2).

$$A' = v \cdot l \tag{2}$$

2.2.1. Surface Characterization

The topographies of the patterned surfaces were characterized using a scanning electron microscope (Philips ESEM). The structure heights were investigated by measuring the structure height h_{st} at different positions on the substrates using confocal microscopy (Sensofar S-Neox).[41]The structure height of the patterns was evaluated using the step height definition, representing the standard type A1 in the norm ISO5436-1.[41] Areas of $200 \times 200\,\mu m^{-2}$ and $100 \times 100\,\mu m^{-2}$ for the spatial periods of $\Lambda = 19\,\mu m$ and $\Lambda = 8\,\mu m$, respectively, were divided into a series of 18 profiles (cross-sections of the interference pattern). These profiles were used to calculate the average values as well as the standard errors for each measurement. In order to determine the effect of the laser treatment on the surface chemistry, the treated surfaces were examined with Energy-dispersive X-ray spectroscopy (EDX, Philips ESEM). Although EDX is of limited use for the precise quantitative determination of material composition in near-surface layers, it can provide useful information for the determination of qualitative changes across periodic patterns as has been previously shown.[42] For performing the EDX analysis, the acceleration voltage was set to 15 kV. The line-scans were realized with a resolution of 284 points/100 µm, corresponding to a separation distance of 352 nm between two data points.

3. Results and Discussion

The DLIP approach was used to produce periodic surface structures on stainless steel with spatial periods of 8 µm and 19 µm. The influence of the pulse-to-pulse (PTP) overlap on the resulting structure height was investigated. **Figure 2** shows SEM images of structured samples spatial periods of 19 µm (Figure 2a,b) and 8 µm (Figure 2c,d) employing a low PTP overlap (Figure 2a,c) and high PTP overlap (Figure 2b,d), respectively. Figure 2a,c show the topography when using a 40 µm PTP feed (60% overlap) while Figure 2b and d show the sample surface when utilizing a PTP feed (99% overlap) of only 1 µm. As expected, the DLIP micro-structures become more pronounced with increasing the number of pulses.

The individual pulses are still visible for large PTP feeds (see Figure 2a and c), while they cannot be distinguished in the surface profile contour for very small feeds (high overlaps, see Figure 2b and d). Particularly, it can be seen in Figure 2a, that the molten material at the interference maxima positions forms two independent melt fronts which follow the thermal gradient perpendicular to the line-like laser intensity distribution. These two fronts of molten material merge with the material release from the neighboring interference maxima at the interference minima regions when increasing the pulse overlap (Figure 2b), especially for shorter spatial periods due to the reduced

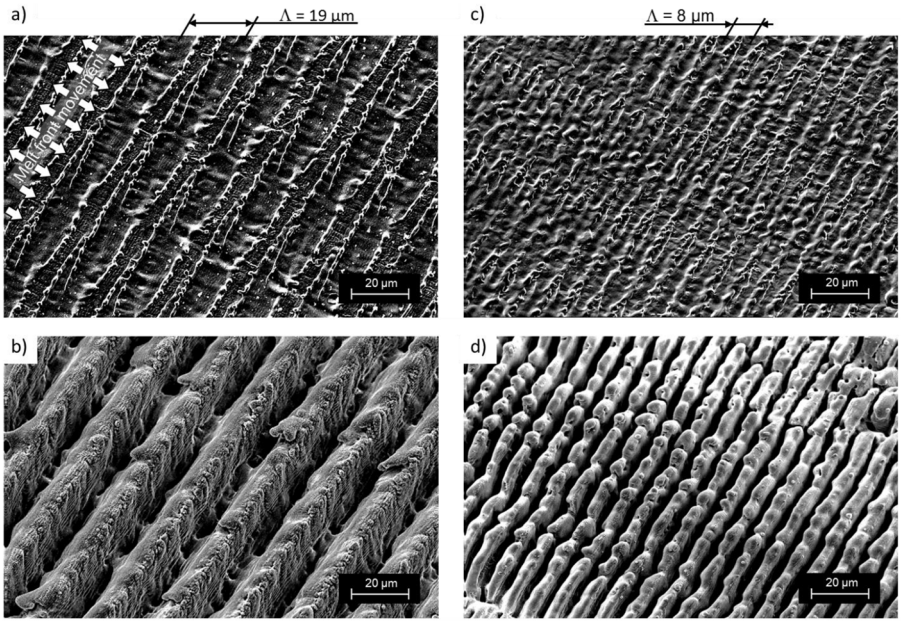

Figure 2. SEM images of treated steel surfaces (X5CrNi18-10/1.4301) with spatial periods of a) $\Lambda = 19\,\mu m$ and 80 % PTP overlap, b) $\Lambda = 19\,\mu m$ and 99 % PTP overlap, b) $\Lambda = 8\,\mu m$ and 80% overlap and c) $\Lambda = 8\,\mu m$ and 99% PTP overlap. The used laser fluence was $3.2\,J\,cm^{-2}$ in all cases.

geometrical distance (Figure 2c). At high PTP overlaps (short PTP feeds), the melt fronts convergence in combination with the large amount of molten material resulting in a significant increase in the structure height, as shown in Figure 2b and d.

Figure 3 shows the confocal microscope images of the same line-like structures as in Figure 2. With shorter PTP feed (higher PTP overlap), considerably deeper structure heights of 8.7 µm and 18.5 µm were achieved for the 8 and 19 µm spatial periods, respectively (see Figure 3b,d). In comparison, the heights of the periodic structures formed with larger PTP feed (lower overlap) reached only structure heights of 3.4 µm and 1.5 µm for the spatial periods of 8 µm and 19 µm, respectively (see Figure 3a,c). The aspect ratios for both periods are very similar when using high overlap conditions (AR of 1.09 and 0.97 for 8 µm and 19 µm period, respectively), at 99% overlap and 3.2 J cm^{-2} laser fluence per pulse (see Figure 3c,d). For low overlap conditions the aspect ratios for both periods differ (AR of 0.42 and 0.08 for 8 µm and 19 µm period, respectively) at 80% overlap at same laser fluence (see Figure 3a,c).

Based on the topographic analysis, the steadiness of structure height of the produced patterns was investigated by evaluating the structure height during the course of the laser process. Since the substrate is moved relative to the DLIP head during the process, the structure height development was determined by measurements at different positions on the processed area on the substrates. The structure heights were measured at the beginning of the process (infeed) and at subsequent positions (dx = 0.5, 1, 2, 3, 4, 5, 10, 20, and 50 mm).

Figure 4 shows the development of the position-dependent structure height during the DLIP process. Figure 4a and b show the structure height evolution for patterns with spatial periods of $\Lambda = 19$ µm, while Figure 4c and d show the structure height evolutions for spatial periods of $\Lambda = 8$ µm. In addition, Figure 4a and c show the influence of different pulse-to-pulse feeds between 1 µm and 20 µm (corresponding to pulse overlaps between 99 % and 80 %, respectively) using the same pulse repetition rate of 5 kHz. Figure 4b and d also show the influence of different pulse repetition rates based on the results obtained with pulse repetition rates from 0.1 kHz to 5 kHz at a fixed pulse-to-pulse feed of 2 µm.

From Figure 4a is visible, that with increasing PTP overlap the structure height increases as well. For high pulse overlaps higher than 98%, maximum structure heights of more than 20 µm (corresponding to aspect ratios of more than 1) are achieved. In all cases, the structure height is always lower at the beginning of the process and gradually increases with increasing distance relative to the process starting point (infeed) until either a steady state condition is reached or even a reduction of the structure height occurs. Different mechanisms can be responsible of the changes in the structure height observed during the process. One possible reason is the heat accumulation which is produced during the laser treatment, meaning that the irradiated steel substrates are heated up.[43,44] Additionally, the produced surface structures on the substrate can have a significant influence on the optical absorption of the laser radiation due to multi-reflections in the generated trenches, which means that a higher amount of energy is coupled in the material as the structure is formed.[45,46] The effect of heat accumulation is further promoted by incubation effects during multi-shot laser ablation.[47] It has been also reported that rippled surface

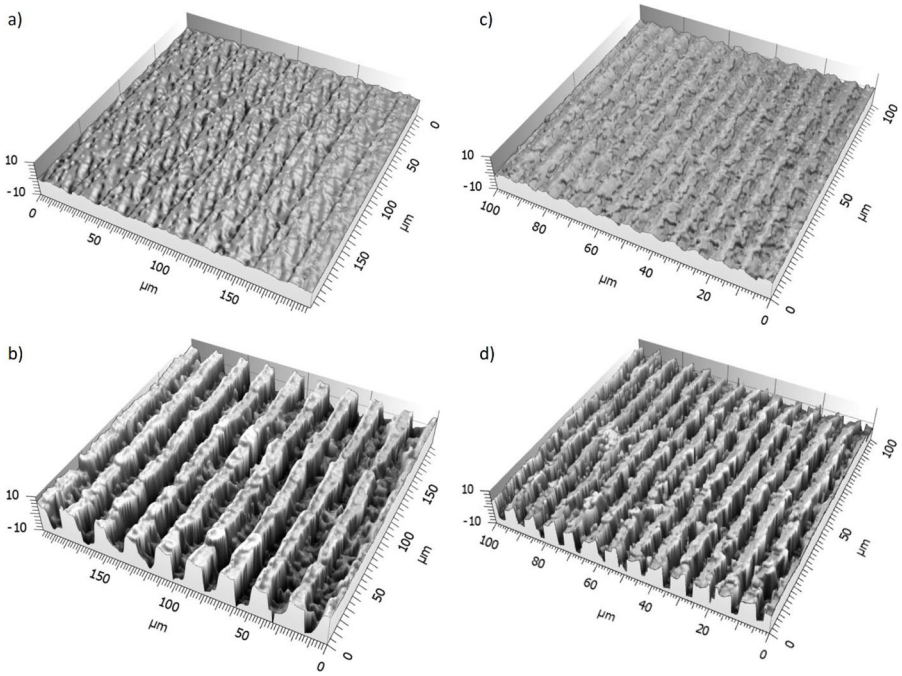

Figure 3. Confocal Microscope images of treated steel substrates (X5CrNi18-10/1.4301) with interference periods of a) $\Lambda = 19$ µm at pulse overlap of 80%, b) $\Lambda = 19$ µm at pulse overlap of 99%, c) $\Lambda = 8$ µm at pulse overlap of 80% and d) $\Lambda = 8$ µm at pulse overlap of 99%. The used laser fluence per pulse was 3.2 J cm^{-2}.

patterns can change the thermal diffusion into the substrate, thus influencing the resulting surface patterns.[48,49]

In general, an increase of the structure height with increasing pulse overlap was observed for both spatial periods: $\Lambda = 19\,\mu m$ (Figure 4a) and $\Lambda = 8\,\mu m$ (Figure 4c). However, for the smaller spatial period ($\Lambda = 8\,\mu m$) a maximum in the structure height was reached at a PTP feed of 2 µm followed by a decrease in structure height for further increasing pulse overlap. For this condition (PTP feed of 2 µm) the evolution of the structure height shows a maximum at the 2 mm position and then subsequently decreases until 10 mm and saturates from 20 mm. Consequently, at the spatial period of $\Lambda = 8\,\mu m$ an optimum condition in terms of structure height can be expected in between the PTP feed values applied. A pulse overlap exceeding this optimum value leads to over-melting, resulting in reduced structure heights.

Regarding the influence of the pulse repetition rate on the structure height for the short spatial period ($\Lambda = 8\,\mu m$, Figure 4d), a similar behavior is observed as for the large periods (Figure 4b), which means that for higher pulse repetition rates higher structures are obtained. However, for the smaller period ($\Lambda = 8$ µm) this dependence shows a minor extent, meaning that the average structure heights achieved with 0.1 kHz is close to that of achieved with 5 kHz (average structure heights 7.4 µm with 0.1 kHz and 8.7 µm with 5 kHz, respectively). A possible explanation for this phenomenon is that for the shorter periods the merging of the melt fronts occurs earlier in the course of the process since melt has to travel a shorter distance.

The results shown in Figure 4 indicate a clear influence of the applied pulse repetition rate on the resulting structure heights since the applied average fluence per pulse is kept constant at $F_{P,av} = 3.2\,J\,cm^{-2}$ during all experiments. The change of the structure height during the laser process indicates that the heat is accumulated at the material if a large number of successive laser pulses is used. Heat accumulation in laser material processing has already been reported, but usually at comparatively higher pulse repetition rates (starting at several hundred kHz).[50–52] Regardless of the applied pulse overlap or pulse repetition rate, the structure heights saturate after a certain distance from the start point. At higher pulse repetition rates, the equilibrium of the structure height occurs later and with higher equilibrium structure heights.

For interpretation of the obtained results, calculations of the thermal evolution due to heat accumulation in the laser-affected zone were carried out according to the model described by Weber et al.[53] (see Equation (3)):

$$T_{Sum,nD}(t) = \frac{Q_{nD}}{\rho \cdot c_p \cdot \sqrt{(4 \cdot \pi \cdot \kappa)}} \cdot \sum_{N=1}^{N_P} \frac{\Theta\left(t - \frac{N-1}{f_L}\right)}{\sqrt{\left(t - \frac{N-1}{f_L}\right)^{nD}}} e^{-\frac{1}{\left(t - \frac{N-1}{f_L}\right)} \frac{r^2_{nD}}{4\kappa}} \quad (3)$$

where Q_{nD} is the residual heat introduced into the material, ρ is the mass density of the material, c_p its specific heat capacity, $\kappa = \lambda_{th} \cdot (\rho \cdot c_p)^{-1}$ is the diffusivity, λ_{th} the heat conductivity, t is time, r the coordinate of space, f_L the laser repetition rate and N_P the number of pulses.

Due to the elongated shape of the laser irradiated area, the solution of the 1D heat flow can be assumed, which gives nD = 1 for the indicator of the dimension. By further setting the volume coordinate r^2_{nD} to zero the following simplified equation is obtained:

$$T_{Sum,nD}(t) = \frac{2 \cdot Q_{Heat}/A}{\rho \cdot c_p \cdot \sqrt{(4 \cdot \pi \cdot \kappa)}} \cdot \sum_{N=1}^{N_P} \frac{\Theta\left(t - \frac{N-1}{f_L}\right)}{\sqrt{t - \frac{N-1}{f_L}}} \quad (4)$$

where Q_{Heat} is the residual heat and A is the irradiated area.

Three different pulse repetition rates of 5 kHz, 1 kHz, and 0.1 kHz were used in the calculations with a constant laser fluence of $3.2\,J\,cm^2$. **Figure 5** shows the calculated temporal

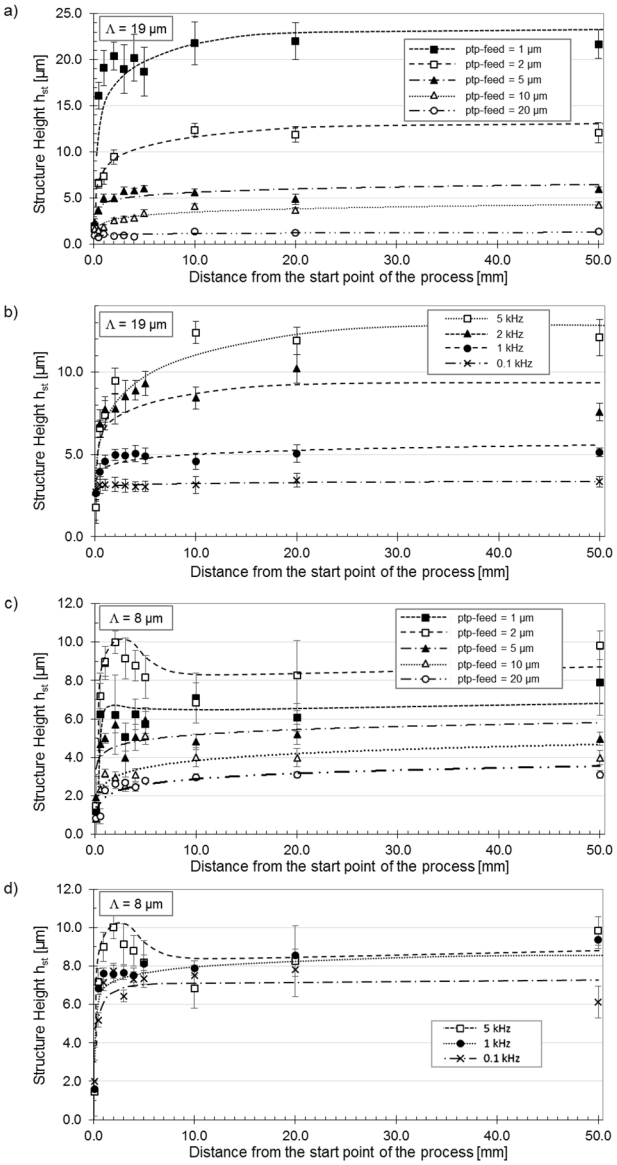

Figure 4. Evolution of structure heights of trench patterns produced with DLIP: a,b) interference period $\Lambda = 19\,\mu m$; c,d) interference period $\Lambda = 8\,\mu m$; a,c) variation of the PTP feed at a fixed pulse repetition rate frep = 5 kHz; b,d) variation of the pulse repetition rate at a fixed PTP feed of 0.002 mm; Material: stainless steel X5CrNi18-10/1.4301. The used laser fluence per pulse was $3.2\,J\,cm^{-2}$.

evolution of the surface temperature for each of the investigated pulse repetition rates. It can be seen that even at repetition rates of 1 kHz, an important accumulation of heat is observed, reaching a temperature increase of 600 K after 100 pulses. A further increase of the rep. rate to 5 kHz produces an increase of ≈1500 K, also after 100 pulses. The calculated temperature evolutions demonstrate that heat accumulation is possible also at relative low repetition rates (KHz range), what in the case of ps laser sources is observed at significantly higher frequencies (e.g., of some MHz).[54,55] This simple calculation clearly demonstrates that the heat accumulation effects can take place in the process used in the experiments and can also explain the variation of the height during the DLIP process.

Figure 6a shows the development of the average aspect ratios of the structure heights for the larger ($\Lambda = 19\,\mu m$) and smaller ($\Lambda = 8\,\mu m$) interference periods as a function of the number of accumulated laser pulses per area. The aspect ratios are calculated as the quotient of the average structure height (from Figure 4) and the corresponding interference period. The observed differences in the structure heights depending on the spatial period and PTP overlap can be interpreted as a result of the melt displacement which is increased due to the accumulation of heat. A generally accepted theory for near-surface melt dynamics during laser processes is provided by Marangoni convection.[56] Furthermore, D'Alessandria et al.[57] have already reported on the different regimes responsible for the pattern formation in DLIP when using ns pulses depending on the applied pulse fluence, which are either Marangoni convection or the recoil pressure. In both cases, the obtained molten metal is driven towards the minima positions. However, the here presented results demonstrate for the first time the possibility of reaching structure heights in the same order of the spatial period (or aspect ratios slightly higher than one).[57] A scheme of the possible structuring mechanism applying the Marangoni convection model for the DLIP using multiple pulses is shown in Figure 6b and c, for long and short periods, respectively. The schema shows that the molten material at the interference maxima positions moves from the hot to the colder peripheral areas due to surface tension gradients induced by the temperature differences. Later, the fronts of molten metal start to merge at the interference minima locations. The application of subsequent laser pulses (with the interference intensity distribution) which is in particular more relevant when using high PTP overlaps results in additional melt leading to patterns with higher aspect ratios. While the structure height can be significantly boosted especially for the larger spatial periods due to stacking of molten material, a stronger increase of the PTP overlap result in a reduction of the structure height for smaller periods due to material over melting (Figure 6c). Overmelting leads to a local collapse of the structures and thus to the emergence of overhang structures (see for example the SEM image of Figure 2d). This would be in accordance with known phenomena in the wake of Marangoni convection, such as the humping phenomenon in laser welding.[58–60] This effect was not observed for larger periods, as in the latter case a larger amount of melt is required due to the longer distances that have to be covered. In fact, overhang structures can be seen as an advantage compared to simple structures. For instance, microtextures with overhang structures can enable to obtain superhydrophobic surfaces, even in materials which are intrinsically hydrophilic.[61,62]

These considerations explain that heat accumulation has similar effect on smaller and larger interference periods, but that for smaller periods the results obtained exceed the state of maximum structure height, whereas this is not the case for the larger periods.

In addition to the topography analysis, EDX measurements were performed for verifying the above described structuring mechanism. **Figure 7** shows the results of an EDX line-scan measured across a DLIP-structure (perpendicular to the interference lines) for iron, oxygen, chromium, and carbon elements. The absolute response of the material during EDX

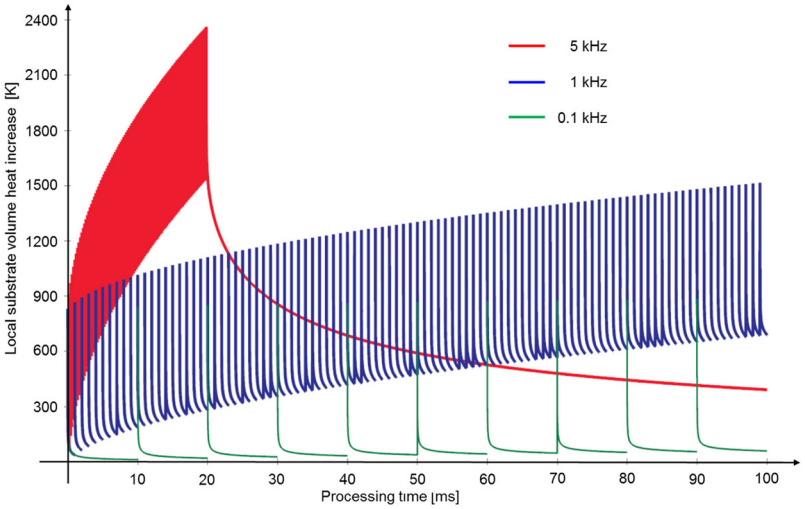

Figure 5. Temporal evolution of the temperature increase ΔTSum,1D on the surface of a semi-infinite body of stainless steel at the location of a one-dimensional source for different repetition rates (5 kHz, 1 kHz, and 0.1 kHz) with equal heat source energy of 16 mJ per laser pulse with pulse durations of $\tau = 10$ ns.

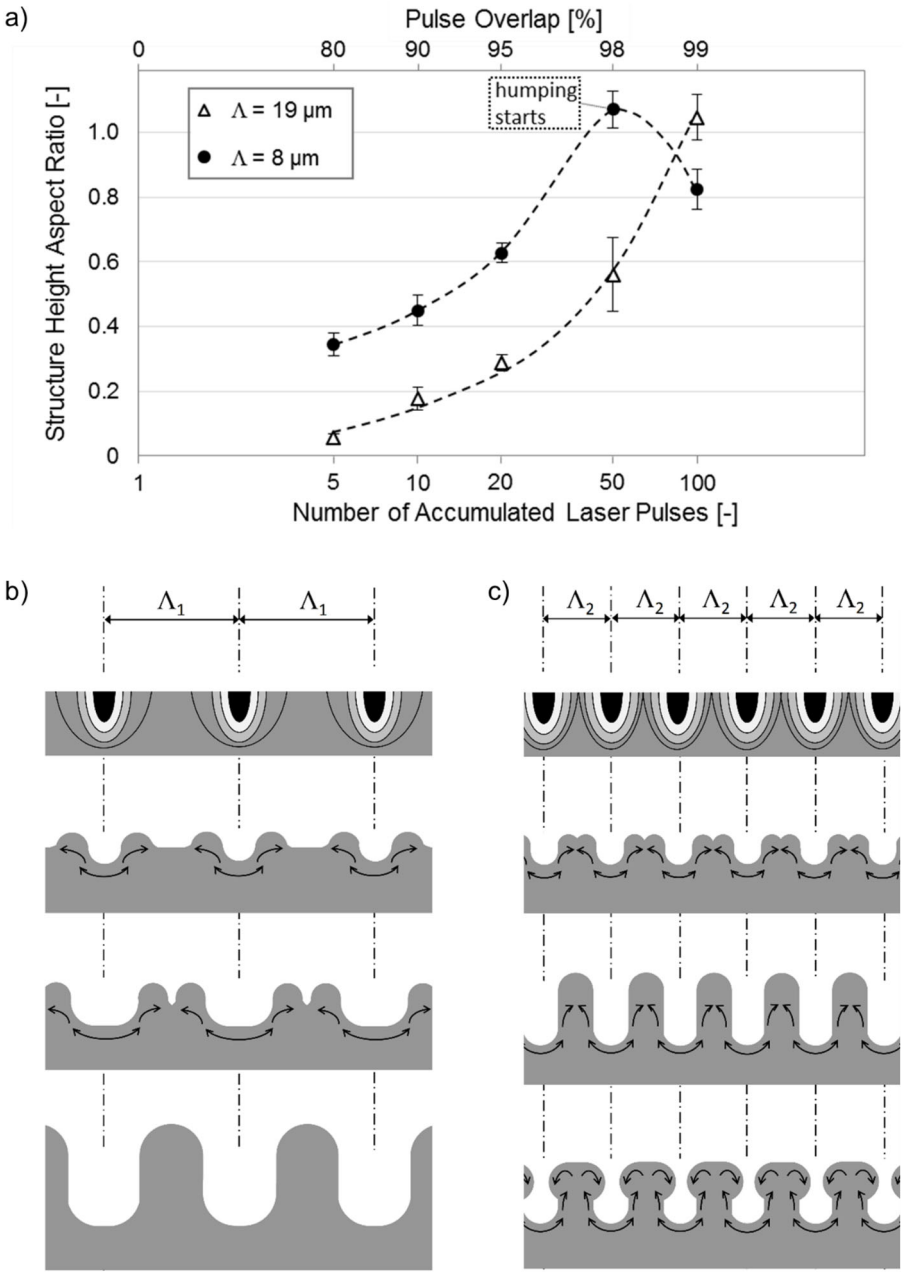

Figure 6. a) Average Structure Height Aspect Ratio as function of Pulse Overlap PO for $\Lambda = 19\,\mu m$ and $\Lambda = 8\,\mu m$ patterns; Schematic representation of the structuring mechanism showing the melt flow in the DLIP processes for b) large and c) short interference periods.

measurements varies very strongly depending on whether the sensing spot strikes in the trenches or on the ridges of the topography. For this reason, for each measurement point of the line scan, the individual percentages of the measured elements were calculated. The gray bars in the background of Figure 7 represent the interference maxima positions which correspond to the locations of the trenches in the produced surface pattern. The image shows that both iron and chromium elements (corresponding to stainless steel) have a higher concentration at the interference maxima positions. Differently, the oxygen content shows a opposite distribution, having a maximal concentration at the interference minima positions. This periodic modulation of the material composition underlines the movement of the melt flow from the interference maxima to minima positions, since the molten metal is longer exposed to the air atmosphere and thus allowing the diffusion of oxygen and finally forming oxides. Both composition distributions for iron and oxygen also show slight double periodic peaks, which is in agreement with the previous explanation and represent the two fronts of molten metal which are finally merged at the interference minima. These effects have been also investigated in the past on steel surfaces which were irradiated using ns pulse

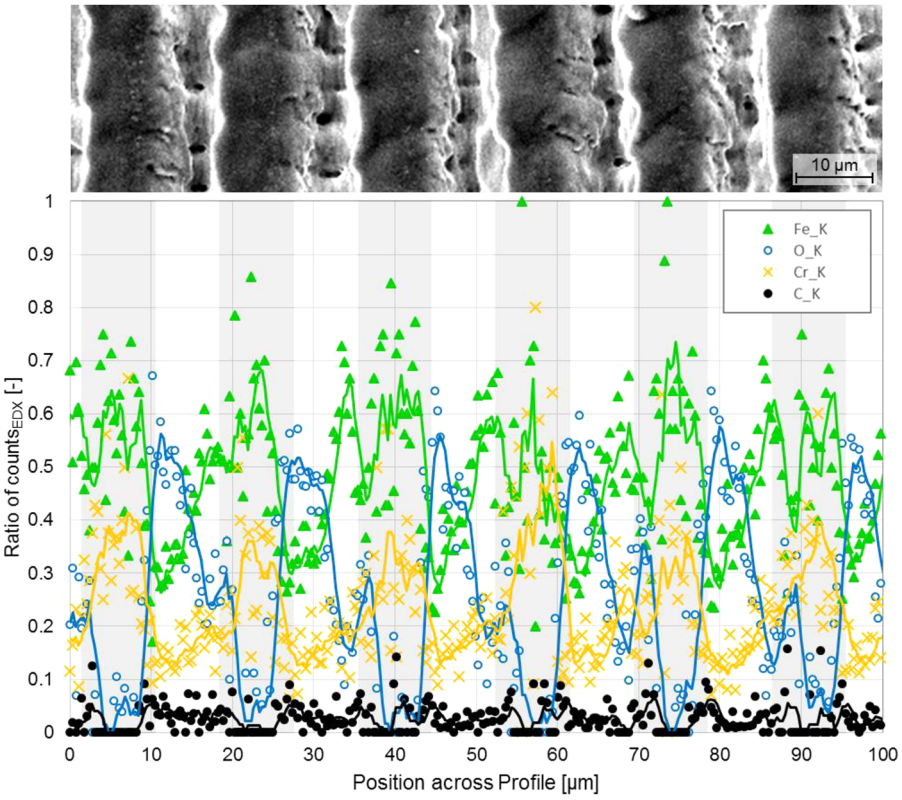

Figure 7. Ratio of the proportions of the most important elements determined as a line diagonally over the cross section of the DLIP trench structures, based on EDX measurement.

DLIP by Rosenkranz et. Al.[63] Using XPS in combination with Ar ion etching as well as atom probe tomography, a sharp interface for transition between the oxidic and metallic state was found for the unpatterned sample, whereas for the laser-irradiated specimens, not only a mixed oxidic state was observed but also an increase of the oxide layer thickness. In addition, this layer consisted on an iron oxide layer on top followed by chromium oxide.[63]

4. Conclusions

In this work, high-speed surface structuring of stainless steel was performed, by developing a DLIP optical configuration producing elongated laser spots containing the interference patterns. This was realized using a modular optics assembly combined the functions of beam splitting (two sub-beams for the production of trench patterns) and beam shaping in order to achieve a rectangular laser spot of 5 mm x 100 µm for interference patterning. Patterns with two different spatial periods (8 µm and 19 µm) were fabricated on stainless steel. The impact of multi-pulsing was investigated by varying the feed rates. It was found that higher overlaps (or a larger amount of pulses) lead to increase the structure heights. Furthermore, it was found that during the DLIP process, a rapid increase in the structure height occurs, particularly at the beginning of the process (≈2 mm after the infeed position). This effect could be explained due to the accumulation of the heat, in particular for repetitions rates of few kHz. Thus, this research work permitted to show for the first time heat accumulation processes using Direct Laser Interference Patterning with ns laser pulses. Depending on the process parameters, aspect ratios slightly higher than one could be realized, which has not been previously achieved using DLIP with ns-pulsed lasers. Particularly for the smaller periods, the melt flow impairs pattern formation due to the overmelting of the material (humping). Finally, a mechanism for the structure formation was presented, which was verified by EDX analyses.

Acknowledgements

This work was supported by the German Research Foundation (DFG) (Programm SPP 1676 "Trockenumformen – Nachhaltige Produktion durch Trockenbearbeitung in der Umformtechnik").

Conflict of Interest

The authors declare no conflict of interest.

Keywords

laser interference, manufacturing, micromachining, surface engineering

Received: February 8, 2019
Revised: March 28, 2019
Published online: April 16, 2019

[1] M. J. Walsh, *AIAA J*. **1983**, *21*, 485
[2] D. W. Bechert, W.-E. Reif, G. Hoppe, *23rd Aerospace sciences meeting* **1985**, 546.
[3] D. M. Bushnell, K. J. Moore, *Annu. Rev. Fluid Mech*. **1991**, *23*, 65.
[4] D. W. Bechert, M. Bruse, W. Hage, *Exp. Fluids* **2000**, *28*, 403.
[5] D. W. Bechert, M. Bruse, W. Hage, R. Meyer, *28th Fluid Dynamics Conf*. **1997**, 1960.
[6] T. Wan Kim, *J. Nanosci. Nanotechnol*. **2014**, *14*, 7562.
[7] G. D. Bixler, B. Bhushan, *J. Colloid Interface Sci*. **2013**, *393*, 384.
[8] J. N. A. Matthews, *Phys. Today* **2008**, *61*, 32.
[9] N. A. Patankar, *Langmuir* **2004**, *20*, 8209.
[10] A. Marmur, *Langmuir* **2004**, *20*, 3517.
[11] W. Barthlott, C. Neinhuis, *Planta* **1997**, *202*, 1.
[12] J. H. Fitton, B. A. Dalton, G. Beumer, G. Johnson, H. J. Griesser, J. G. Steele, *J Biomed Mater Res*. **1998**, *42*, 245.
[13] L. Zhao, S. Mei, P. K. Chu, Y. Zhang, Z. Wu, *Biomaterials* **2010**, *31*, 5072.
[14] C. Liang, H. Wang, J. Yang, Y. Cai, X. Hu, Y. Yang, B. Li, H. Li, H. Li, C. Li, X. Yang, *ACS Appl. Mater. Interfaces* **2013**, *5*, 8179.
[15] A. F. von Recum, T. G. van Kooten, *J. Biomater. Sci. Polym. Ed*. **1996**, *7*, 181
[16] F. Yu, F. Mücklich, P. Li, H. Shen, S. Mathur, C.-M. Lehr, U. Bakowsky, *Biomacromolecules* **2005**, *6*, 1160.
[17] A. Jaggessar, H. Shahali, A. Mathew, P. K. D. V. Yarlagadda, *J. Nanobiotechnol*. **2017**, *15*, 64
[18] L.-C. Xu, C. A. Siedlecki, *Acta Biomaterialia* **2012**, *8*, 72.
[19] N. Lu, W. Zhang, Y. Weng, X. Chen, Y. Cheng, P. Zhou, *Food Control* **2016**, *68*, 344.
[20] A. Vikram Singh, V. Vyas, T. S. Salve, D. Cortelli, D. Dellasega, A. Podestà, P. Milani, W. N. Gade, *Biofabrication* **2012**, *4*, 25001.
[21] C. Díaz, P. Schilardi, M. F. L. de Mele, *Artificial Organs* **2008**, *32*, 292.
[22] A. J. Scardino, E. Harvey, R. de Nys, *Biofouling* **2006**, *22*, 55.
[23] S. Eckhardt, M. Siebold, A. Fabián Lasagni, *Optics Exp*. **2016**, *24*, A553.
[24] C. Fuchs, T. Schwab, T. Roch, S. Eckardt, A. Lasagni, S. Hofmann, B. Lüssem, L. Müller-Meskamp, K. Leo, M. C. Gather, R. Scholz, *Optics Exp*. **2013**, *21*, 16319.
[25] L. Zhou, X. Dong, Y. Zhou, W. Su, X. Chen, Y. Zhu, S. Shen, *ACS Appl. Mater. Interfaces* **2015**, *7*, 26989.
[26] M. L. Brongersma, Y. Cui, S. Fan, *Nature Mater.* **2014**, *13*, 451.
[27] A. Vinčiūnas, S. Indrisiunas, B. Voisiat, *R. Mažeikienė, J. Laser Micro. Nanoeng*. **2013**, *8*, 244.
[28] L. Müller-Meskamp, Y. Hyun Kim, T. Roch, S. Hofmann, R. Scholz, S. Eckardt, K. Leo, A. Fabián Lasagni, *Adv. Mater.* **2012**, *24*, 906.
[29] M. Bieda, C. Schmädicke, T. Roch, A. Lasagni, *Adv. Eng. Mater.* **2015**, *17*, 102.
[30] C. Greiner, A. del Campo, E. Arzt, *Langmuir* **2007**, *23*, 3495.
[31] N. J. Shirtcliffe, S. Aqil, C. Evans, G. McHale, M. I. Newton, C. C. Perry, P. Roach, *J. Micromech. Microeng*. **2004**, *14*, 1384.
[32] A. Fabian Lasagni, D. Benke, T. Kunze, M. Bieda, S. Eckhardt, T. Roch, D. Langheinrich, J. Berger, *Proc. LPM2014* **2014**, 1.
[33] D. J. Guckenberger, T. E. de Groot, A. M. D. Wan, D. J. Beebe, E. W. K. Young, *Lab Chip* **2015**, *15*, 2364.
[34] B. Hyun Kim, S. Hyoung Ryu, D. Ki Choi, C. Nam Chu, *J. Micromech. Microeng*. **2005**, *15*, 124.
[35] H. J. Booth, *Thin Solid Films* **2004**, *453–454*, 450.
[36] A. Lasagni, F. Mücklich, M. R. Nejati, R. Clasen, *Adv. Eng. Mater.* **2006**, *8*, 580.
[37] A. I. Aguilar-Morales, S. Alamri, A. Fabián Lasagni, *J. Mater. Process. Tech*. **2018**, *252*, 313.
[38] P. Shi, D. Li, H. Zhang, Y. Wang, K. Du, *Optics Commun*. **2004**, *229*, 349.
[39] B. Burghardt, H.-J. Kahlert, *Optics for forming a sharp illuminating line of a laser beam*. Veröffentlichungsnr. US Patent 5,721,416.
[40] V. Lang, T. Roch, A. Fabián Lasagni, *Adv. Eng. Mater.* **2016**, *18*, 1342
[41] ISO 5436–1:2000. 2000-03-15. ISO 5436–1:2000(E), *Geometrical Product Specifications (GPS) — Surface texture: Profile method; Measurement standards*.
[42] A. Lasagni, F. Mücklich, *Practical Metallogr.* **2006**, *43*, 1.
[43] G. Raciukaitis, M. Brikas, P. Gecys, M. Gedvilas, in *Proc. of SPIE, 7005*: SPIE Digital Library, **2008**, 70052L.
[44] R. Weber, C. Freitag, T. V. Kononenko, M. Hafner, V. Onuseit, P. Berger, T. Graf, *Phys. Procedia* **2012**, *39*, 137.
[45] L. K. Ang, Y. Y. Lau, R. M. Gilgenbach, H. L. Spindler, *Appl. Phys. Lett*. **1997**, *70*, 696.
[46] D. Bergström, J. Powell, A. F. H. Kaplan, *J. Appl. Phys*. **2007**, *101*, 113504.
[47] F. Di Niso, C. Gaudiuso, T. Sibillano, F. Paolo Mezzapesa, A. Ancona, P. Mario Lugarà, *Optics Exp*. **2014**, *22*, 12200.
[48] T. D. Bennet, D. J. Krajnovic, C. P. Grigoropoulus, P. Baumgart, A. C. Tam, *J. Heat Transfer* **1997**, *119*, 589.
[49] J. M. Prusa, G. Venkitachalam, P. A. Molian, *Int. J. Mach. Tool Manufac*. **1999**, *39*, 431.
[50] F. Brygo, C. Dutouquet, F. Le Guern, R. Oltra, A. Semerok, J. M. Weulersse, *Appl. Surface Sci*. **2006**, *252*, 2131.
[51] H. Wook Kang, H. Lee, A. J. Welch, *J. Appl. Phys*. **2008**, *103*, 83101.
[52] A. Ancona, S. Döring, C. Jauregui, F. Röser, J. Limpert, S. Nolte, A. Tünnermann, *Optics Lett*. **2009**, *34*, 3304.
[53] R. Weber, T. Graf, P. Berger, V. Onuseit, M. Wiedenmann, C. Freitag, A. Feuer, *Optics Exp*. **2014**, *22*, 11312.
[54] B. Luther-Davies, *Optical Eng*. **2005**, *44*, 51102.
[55] S. M. Eaton, H. Zhang, M. Li Ng, J. Li, W.-J. Chen, S. Ho, P. R. Herman, *Optics Exp*. **2008**, *16*, 9443.
[56] J. Mazumder, *Optical Eng*. **1991**, *30*, 1208.
[57] M. D'Alessandria, A. Lasagni, F. Mücklich, *Appl. Surface Sci*. **2008**, *255*, 3210.
[58] U. Gratzke, P. D. Kapadia, J. Dowden, J. Kroos, G. Simon, *J. Phys. D* **1992**, *25*, 1640.
[59] R. Fabbro, *J. Phys. D: Appl. Phys*. **2010**, *43*, 445501.
[60] Y. Kawahito, M. Mizutani, S. Katayama, *J. Phys. D: Appl. Phys*. **2007**, *40*, 5854.
[61] L. Cao, T. P. Price, M. Weiss, D. Gao, *Langmuir* **2008**, *24*, 1640.
[62] S. Shin, J. Seo, H. Han, S. Kang, H. Kim, T. Lee, *Materials* **2016**, *9*, 116.
[63] A. Rosenkranz, L. Reinert, C. Gachot, H. Aboufadl, S. Grandthyll, K. Jacobs, F. Müller, F. Mücklich, *Adv. Eng. Mater.* **2015**, *17*, 1234.

